Chapter 7

Global Dynamics Derived from Synoptic Flow Maps [1]

7.1 Introduction

The Sun's global-scale flows, such as solar differential rotation and meridional circulation, are crucial for understanding solar magnetic cycles and dynamo mechanisms. Large-scale flows, as shown in Gizon, Duvall, & Larsen (2001) and Haber et al. (2002), present information on the dynamics and evolution of active regions. The flow structures of both scales can deepen our understanding of the generation of solar magnetism, and of the birth and evolution of solar active regions.

Solar rotation rates have been widely studied by use of direct Doppler velocity measurements (e.g., Howard & LaBonte, 1980), by tracking photospheric magnetic or supergranular features (e.g., Meunier, 1999), and by both global and local helioseismology (e.g., Thompson et al., 1996; Giles, 1999). The solar cycle variations of solar rotation known as torsional oscillation were first observed by Howard & LaBonte (1980), and then studied by many researchers using different approaches (e.g., Snodgrass, 1985; Howe et al., 2000a; Ulrich, 2001). Torsional oscillation is a phenomenon of mixed faster and slower rotational bands relative to a smooth rotation profile in each hemisphere, with the faster rotational bands residing on the equatorial side of

[1] Most part of this chapter was published in the Astrophysical Journal (Zhao & Kosovichev, 2004)

the solar activity belts. Torsional oscillation is not only found in the photosphere, but has also been detected beneath the solar surface by helioseismology. Analysis of f-mode frequency splitting (Kosovichev & Schou, 1997; Schou, 1999) detected the existence of torsional oscillation extending to a depth of approximately 10 Mm. More recently, it was found that this phenomenon extended to the depth of $0.92R_\odot$ (Howe et al., 2000a), and later found that it might extend down to the tachocline through the entire convective zone (Vorontsov et al., 2002).

The solar meridional circulation is more difficult to observe than the rotational flows, because of its much smaller velocity. Despite difficulties and uncertainties of earlier years, a poleward meridional flow of the order of 20 m/s was eventually found by analysis of Doppler velocity (Duvall, 1979; Hathaway et al., 1996), time-distance helioseismology (Giles et al., 1997) and the ring-diagram analysis (Basu, Antia, & Tripathy, 1999; Haber et al., 2002). More recent studies showed that the meridional flows also vary with the solar cycle. Measurements of acoustic travel times (Chou & Dai, 2001; Beck, Gizon, & Duvall, 2002) implied that, after subtracting a smooth poleward meridional flow profile, the residual meridional flow showed divergent flow patterns around the solar activity belts below a depth of 18 Mm or so. This divergent flow pattern migrates toward the solar equator together with the activity belts. Evidence of meridional flow variations associated with the solar cycle has also been found by the ring-diagram helioseismology (Haber et al., 2002; Basu & Antia, 2003).

The torsional oscillation and meridional flows in the solar interior obtained from helioseismological studies can help us understand turbulence in the solar convection zone. Some numerical simulations (Brun & Toomre, 2002; DeRosa, Gilman, & Toomre, 2002) of the multi-scale turbulent convection inside the solar convection zone, aimed at determining how the differential rotation, torsional oscillations and meridional flows are sustained, and how these global features are related to the turbulence of different spatial scales. It was found that the Reynolds stress might play an important role in sustaining the global-scale flows and transporting the angular momentum in the meridional plane. On the other hand, the differential rotational and meridional flows also provide observational input for numerical models of the solar dynamo (Dikpati & Charbonneau, 1999). It is generally believed that the solar dynamo operates in the tachocline at the base of the convection zone, where the strongest radial rotational shear is located. The poloidal magnetic field of the Sun may be regenerated from the toroidal field by helical turbulence by means of the so-called α-effect (e.g., Stix, 2002). Thus, studies of rotational and meridional flows and their variations associated with the solar cycle are important in understanding the solar dynamo and turbulence in the convection zone.

Time-distance helioseismology measurements and inversions provide a tool to study three-dimensional flow fields in the upper solar convection zone with relatively high spatial resolution. By applying this technique to *SOHO*/MDI Dynamics campaign data (Scherrer et al., 1995), one can map the solar subsurface flows with significantly higher resolution than is obtained from the ring-diagram analysis (e.g., Haber et al., 2002). By averaging such flow maps, both zonal and meridional flows can be derived to compare with results of global helioseismology, direct Doppler measurements and ring-diagram helioseismology. Moreover, a better spatial resolution of time-distance helioseismology enables us to calculate maps of vorticity, from which a latitudinal distribution of vorticity can be inferred. This is important in understanding the α-effect of the solar dynamo theory. Similar studies to derive flow structures just beneath the photosphere have been carried out by f-mode time-distance helioseismology (Gizon, 2003).

In §7.2, we introduce the data reduction and analysis. In §7.3, we present the results for the torsional oscillation, meridional flows, and vorticity distributions with latitude, and show variations of these properties with the solar cycle. In §7.4, we show the residual synoptic flow maps for two solar rotations and discuss the large-scale flow patterns of active regions. Discussions and conclusions follow in §7.5.

7.2 Data Reduction

In every year following the launch of the *SOHO* mission in 1995, the *SOHO*/MDI (Scherrer et al., 1995) has spent about two months in continuous (with only occasional interruptions) full-disk Dynamics Campaigns, observing Dopplergrams with

1-min cadence and 2 arcsec/pixel spatial resolution, thus providing unique data for helioseismological studies. The total number of these campaigns is 7 so far, covering the period from 1996 to 2002, from solar minimum to solar maximum of Solar Cycle 23. The 2003 run was interrupted by too many telemetry gaps to be used for such studies. One useful way to study the large-scale flow structures is to construct synoptic maps of the inferred flows in a way similar to that in which Carrington synoptic magnetic maps are constructed.

In order to make a synoptic flow map for one Carrington rotation, we select a central meridian region 30 heliographic degrees wide in longitude, from $-54°$ to $54°$ in latitude, with continuous 512-minute observation of acoustic oscillations. After remapping the Doppler images by utilizing Postel's projection, and removing the Carrington rotation rate, time-distance measurements are carried out following the descriptions in Giles (1999). Then, data inversions are performed to obtain the horizontal velocities following the procedure described in Chapter 2. This provides one tile for the synoptic flow map. For the next tile, the central meridian region observed 8 hours after the previous region is selected, remapped and processed in the same way. This procedure is repeated until the end of a solar rotation period. In practice, for each solar rotation, approximately 90 tiles of such central meridian regions of size $30° \times 108°$ are obtained, each from continuous 512-minute intervals. The tiles overlap both spatially and temporally. Based on the Carrington coordinate system, these tiles are merged together to form a synoptic flow map, with each specific longitude being overlapped 6 times. The spatial resolution of the resultant flow map is half that of the original MDI full-disk observation, i.e., 0.24 heliographic degrees per pixel. One Carrington rotation is selected for study each year from 1996 through 2002.

The time-distance helioseismology inversions carried out in this study are based on the ray-path approximation. Although an acoustic wave theory for time-distance helioseismology is under development (Birch & Kosovichev, 2000; Gizon & Birch, 2002), it was argued that ray approximation could give credible inversion results with fewer computations (Birch et al., 2001; Jensen et al., 2001). Because of a cross-talk effect between the horizontal divergence and the vertical flows in time-distance measurement (Kosovichev et al., 1997), the weak vertical flows in the quiet solar regions

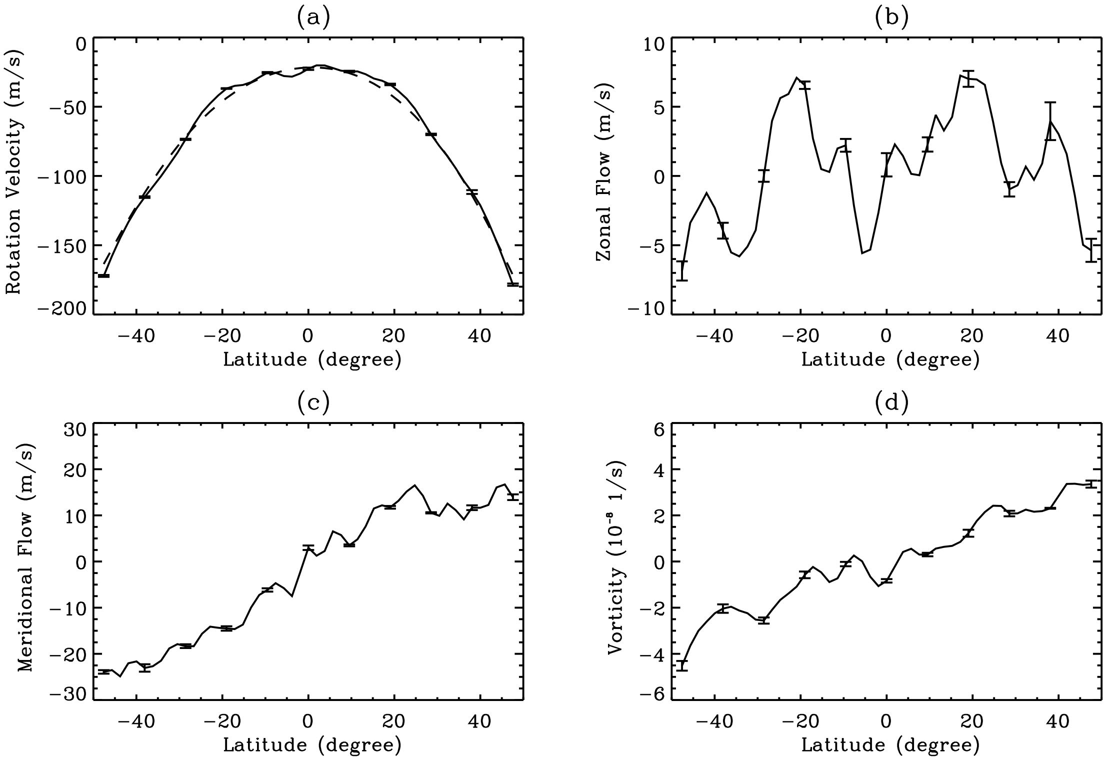

Figure 7.1: (a) Rotation, (b) torsional oscillation (zonal flow), (c) meridional flows and (d) vorticity distribution derived from CR1923 of year 1997 at the depth of 3 – 4.5 Mm. In (a), the solid curve is the rotational velocity displayed after the Carrington rotation rate is subtracted; the dashed line is a fit to the mean rotational velocity (see text). The error bars show the standard deviation of the data from which the rotational velocity is derived. For clarity, only a small number of selected error bars are displayed. In (b), the curve is obtained by subtracting the dashed curve from the solid curve in (a); the error bars may be underestimated, because the error of fitting is not taken into account. In (c) and (d), error bars are obtained and displayed in the same way as in (a). Error bars in Figures 7.2 - 7.4 are obtained and displayed in the same way as here.

derived from our inversions are considered less reliable than the stronger vertical velocity in active regions (Zhao & Kosovichev, 2003b). Therefore, only horizontal velocities are analyzed in this study.

Once the synoptic maps of horizontal velocities at different depths are obtained, the solar rotational and meridional velocities can be derived by averaging the East-West and North-South components of velocities in the synoptic map over longitude for different latitudes. In order to remove fluctuations caused by supergranules, the rotational and meridional velocities are averaged again on a scale of 30 Mm in the latitudinal direction. The vertical component of the vorticity $\omega_z = \partial v_y/\partial x - \partial v_x/\partial y$ (v_x and v_y represent East-West and North-South velocities respectively) is derived at each grid point of the synoptic flow map by employing a standard five-point derivative formula. This provides a synoptic map of the vertical component of vorticity. By applying the same averaging procedure as that used for the rotational and meridional flows, we obtain the vorticity distribution as a function of latitude for different depths. Figure 7.1 shows an example of our inference of rotational velocity, torsional oscillation, meridional flow, and vorticity distribution at a depth of 3 – 4.5 Mm for Carrington Rotation CR1923 in 1997.

7.3 Variations of Torsional Oscillation, Meridional Flow and Vorticity with Solar Cycle

7.3.1 Torsional Oscillation

There are generally two different approaches used to derive torsional oscillations from the inferred rotation rate, one is to subtract a temporal average of measured rotation rates from the whole period of observations from the rotation rate of each observing interval (e.g., Howe et al., 2000a), the other approach is to fit the average rotation rate by a function of $\Omega(\theta) = a_0 + a_1 \sin^2\theta + a_2 \sin^4\theta$, where θ is the solar latitude, then subtract the fitted curve from the individual rotation rate (e.g., Hathaway et al., 1996). There are some differences in the results of these two approaches, as pointed out by Antia & Basu (2000). Because we do not have continuous observations, the second approach is adopted in this study: all seven rotation velocity profiles are averaged to obtain a smoother profile, which is then fitted by the function given above. From our computation, after the subtraction of the standard Carrington rotation rate, the parameters of the fitted function for the rotational velocity are

$a_0 = -21.6$ m/s, $a_1 = -177.6$ m/s and $a_2 = -167.6$ m/s for the depth of 3 – 4.5 Mm, and $a_0 = -6.1$m/s, $a_1 = -233.0$ m/s and $a_2 = -17.8$ m/s for the depth of 6 – 9 Mm. The dashed curve in Figure 7.1a shows the fitted function obtained for the depth interval of 3 – 4.5 Mm. The zonal flows for each rotation is then obtained by subtracting the fitted curve from the rotational velocity profile of the corresponding depth.

The zonal flows, as functions of latitude for two different depth intervals, 3 – 4.5 Mm and 6 – 9 Mm, are shown in Figure 7.2, with the shaded regions indicating locations of the activity belts in both hemispheres. The location of the activity belts is derived from the latitudinal dependence of the mean absolute magnetic field strength obtained for the corresponding Carrington rotation time period by use of MDI magnetograms.

It is important to note that the results of our time-distance helioseismology inversions are consistent with the previous investigations based on different spectroscopic and helioseismic techniques. In particular, in both hemispheres the bands of faster rotation can be found with the activity belts residing on the poleward side of the faster rotation zones. These bands of faster rotation migrate equatorward together with the activity belts as the solar cycle progresses. In addition, the velocity of zonal flows obtained in our time-distance inversions is similar to that obtained by inversion of normal mode frequency splittings (Kosovichev & Schou, 1997; Howe et al., 2000a), and also by the ring-diagram analyses (Basu, Antia, & Tripathy, 1999; Haber et al., 2002). For 1997 – 2002, when solar activity was significant, the faster bands of zonal flows of the order of 5 m/s are prominent, while in 1996 when the Sun was less active, the faster bands are not so obvious, and the maximum velocity variation is also smaller. As one can see, the zonal flows are not symmetric relative to the solar equator.

7.3.2 Meridional Flow

The meridional flows derived for different Carrington rotations are displayed in Figure 7.3a as a function of latitude for two different depth intervals. Generally, the

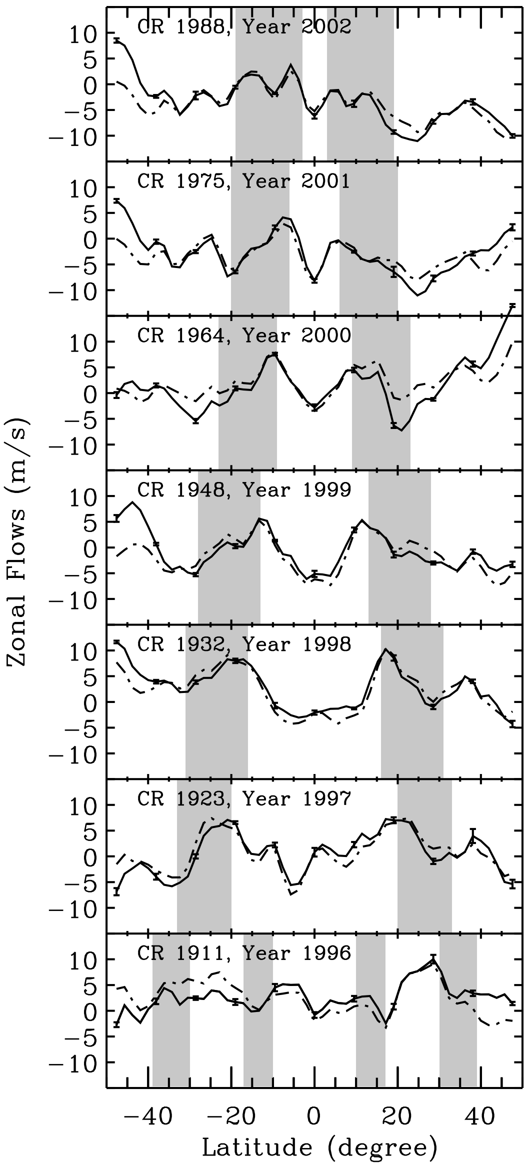

Figure 7.2: Zonal flows obtained at the depths of 3 – 4.5 Mm (*solid curves*) and 6 – 9 Mm (*dash dot curves*) for different Carrington rotations. Note that different rotation profiles have been removed at the two different depth intervals (see text). The shaded regions represent the locations of activity belts. The error bars for the depth of 6 – 9 Mm are not shown but are similarly scaled.

meridional flows are directed poleward with a speed of about 20 m/s, but have some variations in different phases of the solar cycle.

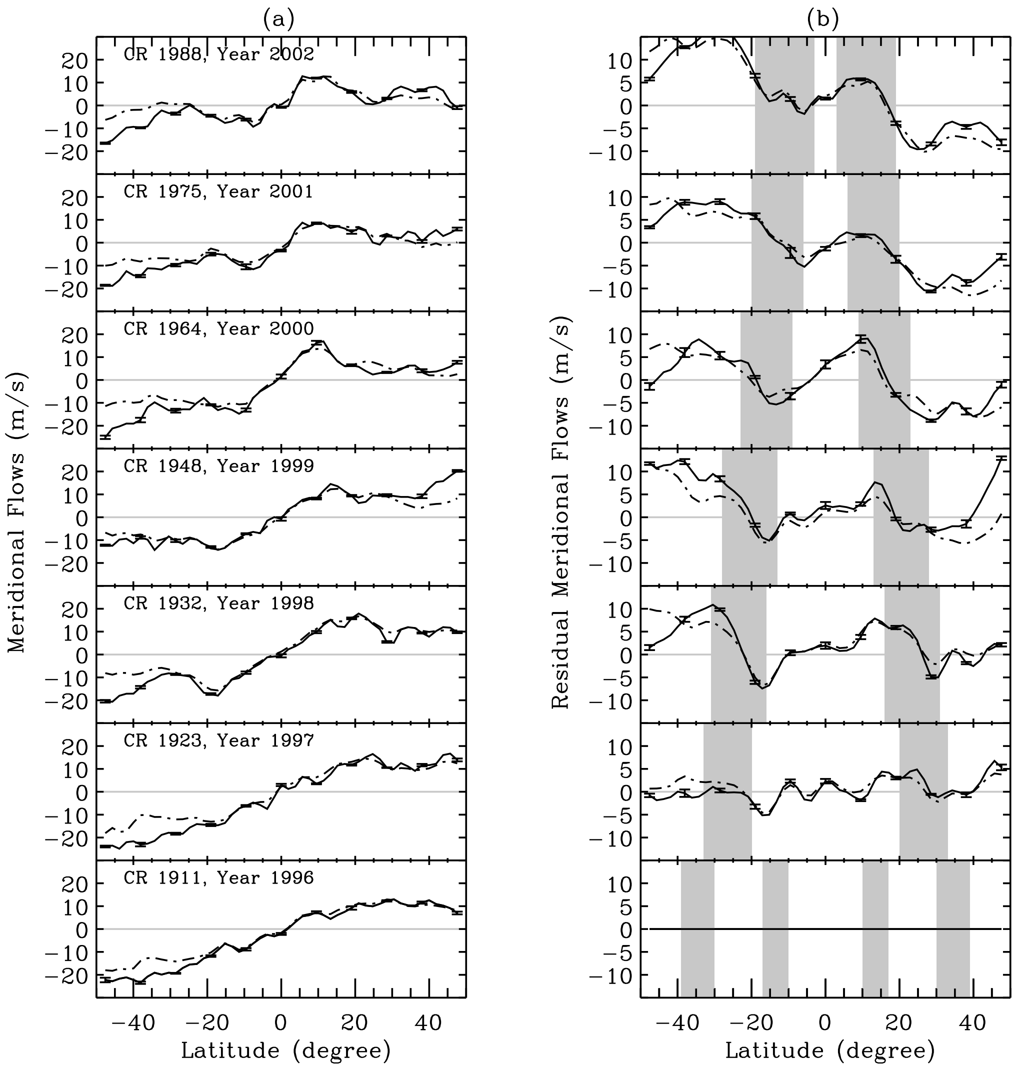

Figure 7.3: (a) Meridional flows obtained from 3 - 4.5 Mm (*solid curves*) and 6 - 9 Mm (*dash dot curves*) for different Carrington rotations. (b) The residual meridional flows after the flows of CR1911 have been subtracted from each rotation. Shaded regions are same as Figure 7.2. The error bars may be underestimated, because the errors from flows of CR1911 are not included.

It has been pointed out that the MDI camera may not be perfectly aligned parallel to the Sun's rotational axis as determined by the Carrington elements (Giles, 1999). A small deviation may cause a leakage of rotational velocity to the meridional direction, thus causing offset to the measurements of meridional flows. It has also been pointed out that the Sun's true rotational axis may differ from that given by the Carrington elements (Giles, 1999). Based on statistics of time-distance measurements, Giles (1999) proposed an empirical formula to make P-angle corrections to the meridional flows (for details, please refer to `http://soi.stanford.edu/papers/dissertations/giles`), which was later used by Schou (2003). Such corrections are employed in this study to adjust the meridional flows derived from our time-distance analysis. We acknowledge that the meridional velocity corrections calculated from the empirical formula may have some uncertainties. Meridional flows shown in Figure 7.3a are after the P-angle corrections.

In order to study variations of the solar meridional flows with the increase of solar activities, we adopt the meridional flows of CR1911 of 1996, obtained during a solar minimum year, as a reference to investigate the changes of meridional flows in the following years, as suggested by Chou & Dai (2001). Thus, we subtract the meridional flow of CR1911 from all the meridional flows of the following years, and display the residual flows in Figure 7.3b.

From Figure 7.3b, we find that residual meridional flows converge toward the activity belts in both hemispheres, and the magnitude of these flows ranges from ~ 2 m/s to ~ 8 m/s. During the studied period, the convergent residual flows migrate toward the equator together with the solar activity belts except in the Northern hemisphere during CR1988 in 2002. The residual flows near the solar surface reveal extra converging components in addition to the poleward meridional flow profile of the solar minimum. The residual flows shown here agree with f-modes analysis near the photosphere (Gizon, 2003), and are in general agreement with findings from the ring-diagram analyses (Haber et al., 2002; Basu & Antia, 2003) that the gradient of the near-equator meridional flows steepen with the development of the solar cycle toward the solar maximum. However, divergent meridional flows from activity belts are found in much deeper solar layers in other time-distance studies (Chou & Dai, 2001; Beck, Gizon, & Duvall, 2002).

It is recognized that the MDI camera was set out of focus in 1996, and also that some focus changes occurred during the period of 1997 to 1999. The focus changes may bring systematic errors into our computations of synoptic flow maps. In order to estimate the error level introduced by the focus changes, we select quiet regions near the solar disk center in the years of 1996 and 1999. Assuming supergranulation in quiet regions remains unchanged in these years, the changes in the magnitude of supergranular divergence may reflect the variations of the velocity measurements caused by the camera focus changes. Our computations show that the changes of the mean magnitude of flow divergence are only 3.6% at the depth of 3 – 4.5 Mm and 0.6% at the depth of 6 – 9 Mm, which are of smaller scales than the error bars in Figure 7.3. On the other hand, the mean acoustic travel time for the shortest time-distance annulus used in our computation shows a change of approximately 4.0% in these two years near the equator, which indicates that the largest possible errors due to the focus changes in the inverted velocity may be approximately 4.0% near the solar surface. The error estimations from the above two different approaches are basically in agreement. Therefore, the selection of the meridional flow of 1996 as a reference does not introduce significant errors in our inferences of the residual meridional flows.

7.3.3 Vorticity Distribution

Figure 7.4a shows the vorticity distribution at two depths for different Carrington rotations. The vorticity distribution seems largely to be a linear function of latitude, with some fluctuations for all years. This indicates that the global-scale vorticity mainly results from the differential rotation, in which the derivative of the term $\sin^2\theta$ has the largest contribution. We then compute the vorticity contributed from the fitted rotational velocities obtained from Section 3.1, and subtract the vorticity function from the vorticity distribution of each rotation to study the deviation of the vorticity distribution from that caused by the mean differential rotation.

The latitudinal distributions of the residual vorticity obtained after subtracting the derivative of mean differential rotation are presented in Figure 7.4b. It is found that in the Northern hemisphere, the residual vorticity usually displays a peak within the activity belt, and two valleys on both sides of the peak. However, in the Southern hemisphere, the residual vorticity usually displays a valley within the activity belt except in CR1988. The peaks and valleys of the residual vorticity in the activity belts

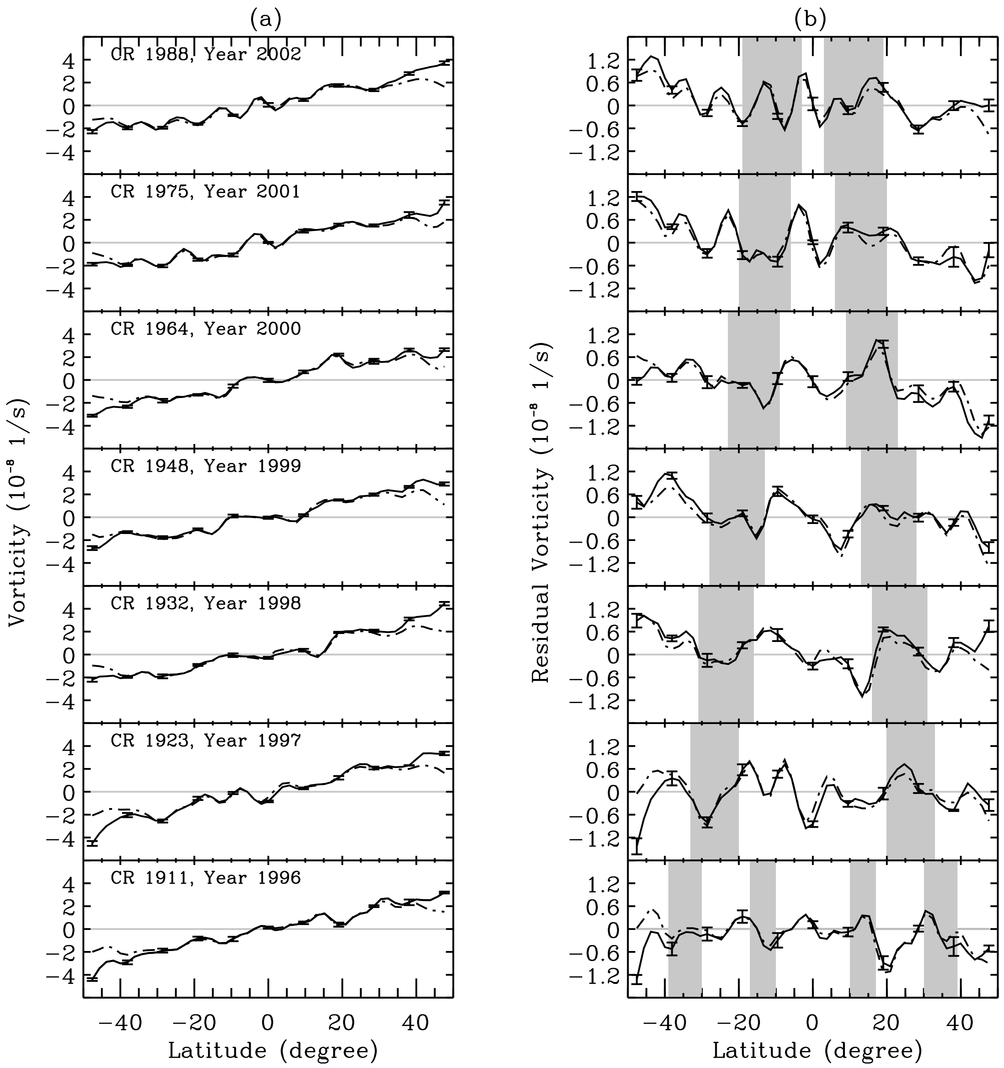

Figure 7.4: (a) Same as Figure 7.3a but for vorticity; (b) The residual vorticity after the vorticity caused by the mean differential rotation is subtracted from the vorticity distribution of each Carrington Rotation. The shaded regions represent the locations of solar activity belts. The error bars may be underestimated because the errors from the derivative of the mean differential rotation are not included.

migrate together with the solar activity belts as the solar cycle progresses.

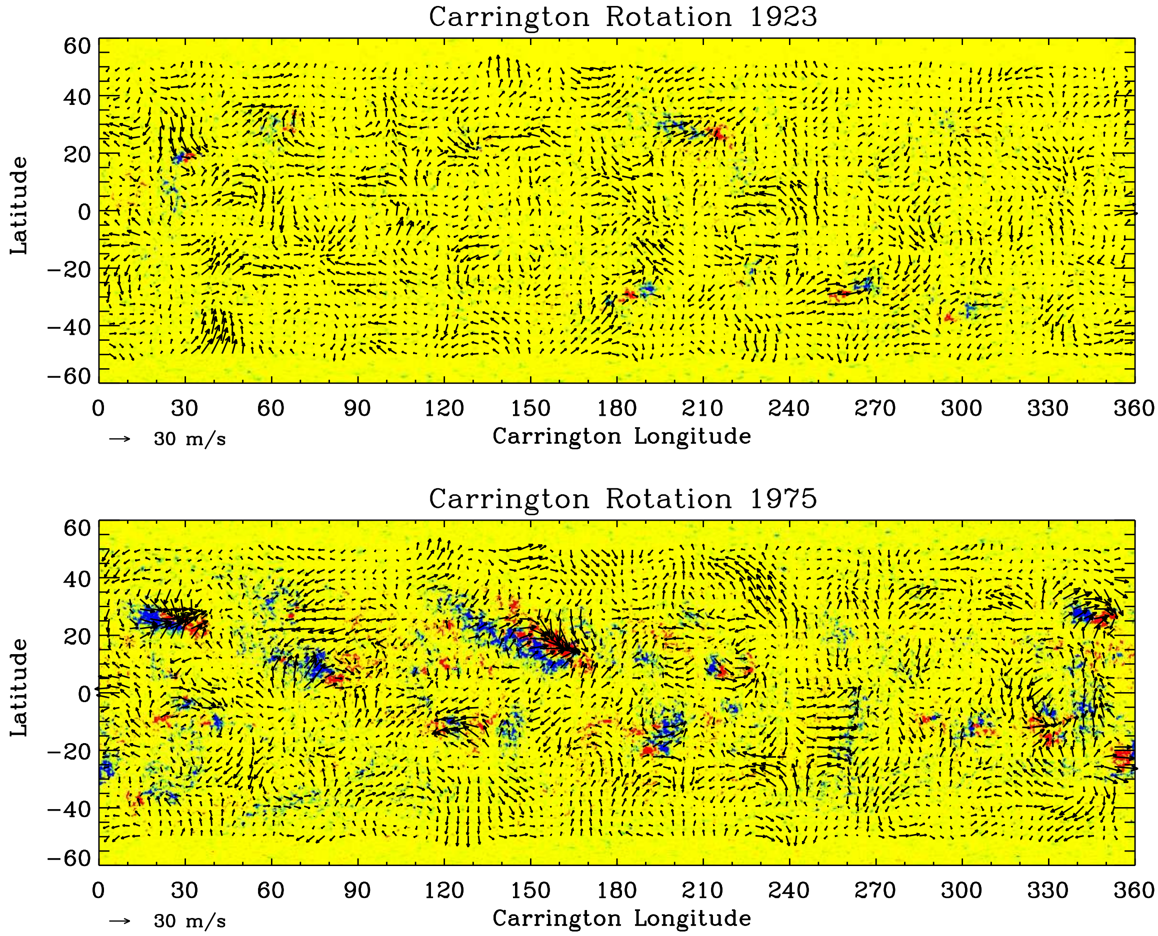

Figure 7.5: Synoptic maps for the residual flows at the depth of 0 – 3 Mm for CR1923 (*above*) and CR1975 (*lower*).

7.4 Residual Flow Maps

From the synoptic flow maps obtained by the time-distance analysis, we have derived the mean rotational and meridional flow velocities. We remove the mean rotational and meridional velocities from the synoptic flow maps and obtain residual synoptic flow maps, which can reveal dynamics in local areas (Gizon, Duvall, & Larsen, 2001).

The residual synoptic flow maps are made for each Carrington rotation by merging together every 512-minute time-distance flow map after the mean differential rotation rates and meridional flows calculated separately for each rotation have been removed.

These flow maps have a high spatial resolution of 2.90 Mm per element and contain 1512×462 data points. However, in order to show the large-scale flows in this article and to make comparison with flow maps from ring-diagram analysis (Haber et al., 2002), we derive a larger scale flow velocity by averaging all the high spatial resolution velocities inside a square region with a side length of approximately $15°$, taking into account spatial apodization of the ring analysis. Thus, we obtain larger scale flow maps of 96×48 data points separated in longitude and latitude by $3\overset{\circ}{.}75$. Significant spatial overlapping has been applied in this averaging procedure, and this simulates the synoptic flow maps obtained by the ring-diagram techniques (Haber et al., 2002). A more detailed comparison between the ring-diagram results and the time-distance inferences shown here is being carried out (Hindman et al., 2003).

Figure 7.5 presents the residual synoptic flow maps for Carrington Rotations 1923 and 1975 at the depth of 0 – 3 Mm. Such maps display the flow patterns, especially the local variations, near the solar surface. Apparently, areas inside and around active regions show stronger and more systematic flows converging toward the active regions. The map of Carrington rotation CR1923, which was taken during a solar minimum year, has fewer active regions and shows weaker and less systematic flow patterns than the CR1975 map that has stronger magnetic activity. It is noticeable that even small active regions with relatively weak magnetic field have large-scale plasma flows toward them.

The flow fields beneath and around sunspots have been studied using MDI high-resolution and full-disk data (Chapter 3 of this dissertation; Kosovichev, Duvall, & Zhao, 2002). The converging and downward flows were found from near the photosphere to about 5 Mm in depth, the divergent flows were discovered deeper than 5 Mm. However, the larger scale flows beneath active regions may not have same structures as the small-scale flows beneath sunspots.

In Figure 7.6, we display the large-scale flow maps at two different depths around active region AR9433 during its passage of the central meridian in CR1975 taken in April, 2001. Near the solar surface at the depth of 0 – 3 Mm, converging flows can be found toward the neutral line of this huge active region with a speed of approximately 40 m/s. This is generally consistent with the finding of converging flows toward the

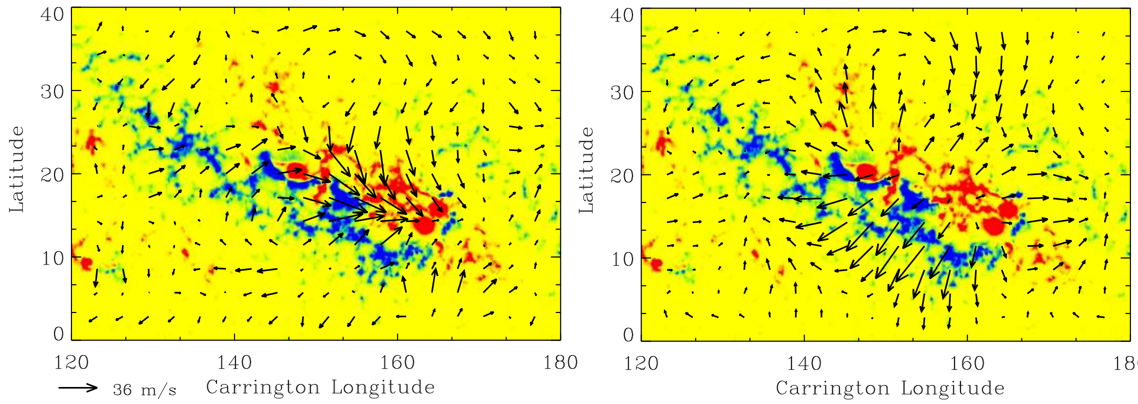

Figure 7.6: The large-scale averaged flow maps for a large active region AR9433 at two different depth intervals: 0 – 3 Mm *(left)* and 9 – 12 Mm *(right)*.

sunspot center (see Chapter 3), but with much smaller speed. However, the large-scale converging flow pattern of this active region seems to remain deeper than the small-scale converging flow pattern of sunspots. The large-scale divergent flows are only found beneath 9 Mm as shown in the right panel of Figure 7.6, while for the small-scale flows of sunspots this happens at a rather shallow depth of 5 Mm. Similar studies on active regions by ring-diagram analysis (Haber, Hindman, & Toomre , 2003) found that converging flows of active regions extended down to 10 Mm, even 16 Mm in some cases, which is much deeper than what we found. For studying flows around active region it is important to obtain small-scale flow maps, because the flows vary on relatively small scales.

7.5 Discussion and Conclusion

Using time-distance helioseismology measurements and inversions, we have obtained high-resolution synoptic horizontal flow maps for several solar rotations covering the first half of Solar Cycle 23 from minimum to maximum. The global-scale zonal and meridional flows, and the vorticity distributions are derived by averaging these high resolution data. Large-scale synoptic flow maps and large-scale flow patterns around active regions are obtained as well.

We find from this study that there is one, sometimes two, faster rotational bands residing in each hemisphere, as already shown in many previous studies (e.g., Howard & LaBonte, 1980; Kosovichev & Schou, 1997; Howe et al., 2000a). The activity belts are located at the poleward side of the faster zonal bands, and they migrate together towards the solar equator with the development of the solar cycle towards solar maximum. The zonal flows in the Southern and Northern hemispheres are not symmetrical, which was also pointed out in previous time-distance and ring-diagram analyses (Giles, 1999; Basu, Antia, & Tripathy, 1999; Haber et al., 2002).

From the meridional flows shown in Figure 7.3a, we find that flows of an order of 20 m/s remain mainly poleward at different depths through the whole period. Haber et al. (2002) reported an additional submerged cell seen in the Northern hemisphere from 1999 through 2001 beneath the depth of 6 Mm or so. However, in our study we do not see the equatorward flows occurring at the corresponding latitudes of the Northern hemisphere during these years, except perhaps in 2001 when some very small negative flows seem to appear above the latitude of 35° in the Northern hemisphere at the depth of 6 – 9 Mm. But it is possible that this small equatorward flow result from the inaccuracy of our P-angle corrections. Without the P-angle corrections, the meridional flows from our inversions also show the additional submerged cell in some deeper layers as claimed by Haber et al. (2002). This may indicate that the submerged meridional cell reported by Haber et al. (2002) resulted from the misalignment of the MDI instrument relative to the Sun's rotation axis. However, we cannot exclude the possibility that the reversed meridional flow cell may exist deeper than 12 Mm where our analyses have not reached. Furthermore, we should also recognize that although the meridional flow corrections give us reasonable results as shown in Figure 7.3a, there may be some other currently unknown sources that may affect the inference of meridional flows by local helioseismology techniques.

The residual meridional flows shown in Figure 7.3b present us some interesting results. By performing time-distance measurements, Chou & Dai (2001) and Beck, Gizon, & Duvall (2002) detected migrating outflows from the solar activity belts in addition to the normal poleward meridional flows. However, from the measurements of acoustic travel times alone without doing inversions, it is difficult to determine the depth of the divergent flows. Based on our inversion results and the annulus ranges used in the two papers mentioned above, we estimate that divergent flows exist below a depth of approximately 18 Mm. The results shown in Figure 7.3b of our study also present a migrating signature of the residual meridional flows, but with a converging flow toward the activity belts from the solar surface to the depth of at least 12 Mm. This agrees with the results of converging residual meridional flows just below the photosphere, at a depth of 1 Mm or so, obtained by the f-modes analysis (Gizon, 2003). In addition, this signature is also generally consistent with the finding that the gradient of meridional flows steepens near the equator (Haber et al., 2002), and is also consistent with the variations of meridional flows after symmetrizing the flow structures of both hemispheres (Basu & Antia, 2003). From all these observations, we have a general picture of the residual meridional flows relative to the solar minimum: from the photosphere to the upper convection zone of approximately 12 Mm the residual meridional flows converge toward the solar activity belts, and below the depth of approximately 18 Mm the residual meridional flows diverge from the activity belts, thus forming circulation cells around the activity belts. Downdrafts are expected in the activity belts from the photosphere to the upper convection zone. These flows migrate toward the solar equator together with the activity belts as the solar cycle progresses. This general picture is similar to the schematic diagram proposed by Snodgrass (1987) and the theoretical prediction by Kleeorin & Ruzmaikin (1991). However, in this case, there must exist a depth where the converging flows turn over into the divergent flows, and detecting this turning point may be an important step in better understanding the mechanism of the formation of these flows. From the study of Chou & Dai (2001) and this investigation, the transition point is probably located somewhere between 12 and 18 Mm.

The extra meridional circulation cells associated with the magnetic activity in addition to the widely known poleward single cell pattern may have some interesting implications for dynamo theory. It is recognized that meridional circulation may play an important role in the regeneration of poloidal magnetic field and angular momentum transport (Wang, Sheeley, & Nash, 1991); accurate measurements of meridional flows have helped to build numerical simulations of the solar dynamo (Dikpati &

Charbonneau, 1999). The extra meridional circulation cell found in this study may add some new contents to these simulations, because this indicates that the meridional flows do not stay unchanged during the solar cycle, but vary with the location of the solar activity belts. Moreover, the additional converging flow structure may help transport more magnetic flux to the activity belts, but hamper the flux transported to the polar regions. On the other hand, the converging flows and the implied downdrafts in the activity belts may result from the hydrodynamic effects associated with cooling in magnetic regions, as recently discussed in a geostrophic flow model (Spruit, 2003). Or perhaps, the converging flows and downdrafts are just a global-scale manifestation of the strong converging flows and downdrafts in regions with strong magnetic fields.

The vorticity distribution is largely a linear function of latitude, with small deviations. Our calculations in Figure 7.4 show that the vorticity results mainly from the differential rotation. The vorticity inside supergranules and at the supergranular boundaries caused by the Coriolis force is approximately one order of magnitude smaller than vorticity generated by the differential rotation; this is apparently due to the cancellation of the opposite sign of vorticity in the supergranular converging and divergent flow regions. Since the flow vorticity is directly related to the α-effect, this may imply that in the upper convection zone, the local vorticity caused by the Coriolis force does not make a significant contribution to the α-effect on the global-scale compared to the differential rotation.

In this chapter, we have also presented large-scale flow maps for one large active region AR9433. It is found that the flows near the photosphere converge around both individual sunspots and the whole active region. However, for individual sunspots, divergent flows are found below the depth of 5 Mm, while for the whole active region, large-scale divergent flows are only found below the depth of approximately 9 Mm. This may imply that large active regions have deeper roots and deeper thermal and dynamical structures than individual sunspots. Combining the residual meridional flow structures discussed above, we find that converging flows are replaced by divergent flows beneath 5 Mm for individual sunspots, and the turning point for large active regions is at approximately 9 Mm, while the transition is located deeper than

12 Mm for the residual meridional flows at the solar activity belts. The underlying mechanisms for the converging and diverging flows around sunspots, active regions and activity belts are not well understood; it is possible, however, that the flows are the manifestation of a single mechanism being exhibited on different spatial scales.

As a summary, time-distance helioseismology has provided us with new information about solar dynamics in the upper convection zone and its relation to solar activity. We have found an extra meridional circulation cell around the solar activity belts, determined the distribution of vorticity, and studied the large-scale flows around a large active region. It is intriguing that despite the turbulence in the solar convection zone, it seems that the dynamics are also highly organized on large scales, which can be correlated with solar magnetic activity.